Correspondence to:
J. M. C. Plane,
j.m.c.plane@leeds.ac.uk

The Meteoric Ni Layer in the Upper Atmosphere

Shane M. Daly[1] , **Wuhu Feng[1,2]** , **Thomas P. Mangan[1]** , **Michael Gerding[3]** , and **John M. C. Plane[1]**

[1]School of Chemistry, University of Leeds, Leeds, UK, [2]NCAS, University of Leeds, Leeds, UK, [3]Leibniz Institute of Atmospheric Physics, Kühlungsborn, Germany

Abstract The first global atmospheric model of Ni (WACCM-Ni) has been developed to understand recent observations of the mesospheric Ni layer by ground-based resonance lidars. The three components of the model are: the Whole Atmospheric Community Climate Model (WACCM6); a meteoric input function derived by coupling an astronomical model of dust sources in the solar system with a chemical meteoric ablation model; and a comprehensive set of neutral, ion-molecule, and photochemical reactions pertinent to the chemistry of Ni in the upper atmosphere. In order to achieve closure on the chemistry, the reaction kinetics of three important reactions were first studied using a fast flow tube with pulsed laser ablation of a Ni target, yielding $k(\text{NiO} + \text{O}) = (4.6 \pm 1.4) \times 10^{-11}$, $k(\text{NiO} + \text{CO}) = (3.0 \pm 0.5) \times 10^{-11}$, and $k(\text{NiO}_2 + \text{O}) = (2.5 \pm 1.2) \times 10^{-11}$ cm^3 molecule^{-1} s^{-1} at 294 K. The photodissociation rate of NiOH was computed to be $J(\text{NiOH}) = 0.02$ s^{-1}. WACCM-Ni simulates satisfactorily the observed neutral Ni layer peak height and width, and Ni$^+$ measurements from rocket-borne mass spectrometry. The Ni layer is predicted to have a similar seasonal and latitudinal variation as the Fe layer, and its unusually broad bottom-side compared with Fe is caused by the relatively fast NiO + CO reaction. The quantum yield for photon emission from the Ni + O$_3$ reaction, observed in the nightglow, is estimated to be between 6% and 40%.

Plain Language Summary Around 30 t of cosmic dust particles enters the Earth's atmosphere every day. A fraction of these particles heat through collisions with air molecules to the point where they melt and evaporate. This process of ablation injects a variety of metals into the region between 80 and 110 km, where the metals occur globally as layers of atoms and ions. The metal Ni is present in cosmic dust in metallic grains as an alloy with Fe. In the past decade, the layer of Ni atoms has been observed for the first time, complementing earlier measurements from rockets of Ni$^+$ ions, and a faint contribution to the Earth's nightglow from excited NiO molecules. In this study we present the first atmospheric model of nickel, which is possible following an extensive laboratory program to measure the rates of the reactions that Ni species are likely to undergo in the upper atmosphere, as well as the ablation of Ni from meteoritic fragments. The model successfully simulates the observed layers of Ni and Ni$^+$ and shows that the production of photons from the reaction between Ni and O$_3$ must be relatively efficient.

1. Introduction

The mesosphere lower thermosphere (MLT) is a region in the Earth's atmosphere (70–120 km) where layers of metal atoms and ions occur as a result of meteoric ablation (Feng et al., 2013; Plane et al., 2015, 2018). Ni$^+$ ions (^{58}Ni$^+$ and ^{60}Ni$^+$) were first measured using a quadrupole mass spectrometer flown on a sounding rocket (Krankowsky et al., 1972), with subsequent measurements throughout the 1970s and 1980s (Grebowsky & Aikin, 2002; Kopp, 1997). Chemiluminescence from electronically excited NiO, produced from the highly exothermic reaction between Ni and O$_3$, was detected as a broad continuum in the visible part of the nightglow spectrum (440–670 nm) by Evans et al. (2011) using the OSIRIS spectrograph on the Odin satellite (Llewellyn et al., 2004) and the GLO-1 spectrograph on the Space Shuttle (Broadfoot & Bellaire, 1999).

During the past decade, the Ni layer has been observed in two lidar studies. Measurements of Ni were first made at Chatanika, Alaska (65°N, 147°W) on two nights in midwinter 2012 by probing the Ni(^{3}F$_4$-^{3}D) transition at $\lambda_{\text{air}} = 336.96$ nm (Collins et al., 2015). The peak density was 1.6×10^4 cm^{-3} at 87 km, with a column abundance of 2.7×10^{10} cm^{-2}. Compared with Fe, another transition metal that should be injected through meteoric ablation over a similar height range (Carrillo-Sánchez et al., 2020), the Fe:Ni column abundance ratio was only 1.2:1, which is much smaller than the carbonaceous Ivuna (CI) chondritic ratio of 18:1

Figure 1. Schematic diagram of Ni chemistry in the MLT arising from meteoric ablation. Ionized neutral Ni species are shown in blue and green boxes, respectively. Red arrows indicate reactions measured in this study.

(Asplund et al., 2009) (the CI ratio is regarded as the closest in composition to interplanetary dust; Jessberger et al., 2001).

This surprising discrepancy prompted a further lidar study at Kühlungsborn, Germany (54°N, 12°E) on six nights between January and March 2018, using the same spectroscopic transition as Collins et al. (2015), as well as the stronger Ni(a^3D_3-$^3F_4$) transition at λ_{air} = 341.48 nm (Gerding et al., 2019). The Ni densities were found to be much lower, with peak densities ranging from 280–450 cm^{-3} and column abundances from $(3.1–4.9) \times 10^8$ cm^{-2}. This gave a Fe:Ni ratio of 38 ± 11, a factor of 2.4 ± 0.7 times larger than the CI ratio, and a factor of 32 larger than that determined by Collins et al. (2015). However, both studies found that the Ni layer was broader than the Fe layer on the bottom-side of the layer. The Ni layer also appeared to exhibit more short-term variability than Fe, with the peak density of Ni varying by 55% in just 15 min (Gerding et al., 2019), compared with the Fe peak density varying by 45% over 6 hr (Bills & Gardner, 1990).

Recently, we investigated the ablation of Ni from meteoritic fragments using the Meteoric Ablation Simulator (MASI): the evaporation of Ni and Na were measured by laser-induced fluorescence (LIF) as size-selected fragments were heated at rates that simulated atmospheric entry (Bones et al., 2019). The experimental results were then used to produce a new version of the Leeds Chemical ABLation MODel (CABMOD-3), where the Ni is treated as being in Ni-Fe-S grains, which are separated from the bulk Fe-Mg-SiO$_4$ phase (Carrillo-Sánchez et al., 2020). Both the MASI data and CABMOD-3 simulations show that the ablation of Ni (as well as metallic or sulfide Fe) occurs rapidly at a relatively low temperature of ~2200 K, before the bulk silicate phase of Fe has ablated. The Meteoric Input Function (MIF) of Ni was then estimated by combining CABMOD with the Zodiacal Cloud Model (ZoDy) (Nesvorný et al., 2011), which provides the mass, velocity, and radiant distributions for cometary and asteroidal particles in the near-Earth environment.

The ratio of the MIFs for Fe and Ni is predicted by the CABMOD-ZoDy coupled model to be 16:1, which is close to the CI ratio of 18:1 but ~15 times greater than the lidar observations of Collins et al. (2015). This might indicate a high Ni enrichment in cosmic dust particles, but that contradicts the analysis of meteoritic fragments in our laboratory (Bones et al., 2019), and the Fe:Ni ratio measured in cosmic dust particles which survived atmospheric entry (Arndt et al., 1996). The CABMOD-ZoDy ratio is a factor of ~0.42 times smaller than the Kühlungsborn lidar-measured ratio of 38:1 (Gerding et al., 2019), which may suggest that Ni is converted to long-term atmospheric sinks more efficiently than Fe (Carrillo-Sánchez et al., 2020). In comparison, the Fe$^+$:Ni$^+$ ratio measured between 85 and 100 km, measured during eight rocket flights, is 20^{+13}_{-8}, which is close to the ratio of the Fe and Ni MIFs (Carrillo-Sánchez et al., 2020).

We have also recently carried out a series of kinetic studies of the relevant neutral (Mangan et al., 2019) and ion-molecule (Bones et al., 2020) chemistry of the metal. Figure 1 illustrates the reactions connecting neutral Ni species (green boxes) and ionized species (blue boxes). In the MLT, Ni is oxidized by O$_3$ and O$_2$ (Mangan et al., 2019):

$$Ni + O_3 \rightarrow NiO + O_2 \tag{R1}$$

$$Ni + O_2\ (+M) \rightarrow NiO_2, \text{ where } M = N_2 \text{ or } O_2 \tag{R2}$$

$$NiO + O_3 \rightarrow NiO_2 + O_2 \tag{R3a}$$

$$\rightarrow Ni + 2O_2 \tag{R3b}$$

By analogy with other meteoric metals (Plane et al., 2015), the resulting oxides are then likely to be reduced back to Ni by O and CO (red arrows in Figure 1):

$$NiO + O \rightarrow Ni + O_2 \tag{R4}$$

$$NiO + CO \rightarrow Ni + CO_2 \tag{R5}$$

$$NiO_2 + O \rightarrow NiO + O_2 \tag{R6}$$

As shown in Figure 1, NiO and NiO_2 can react further with O_3, O_2, CO_2, and H_2O to form higher oxides, carbonates, and hydroxides. These are eventually recycled to Ni through H atom reactions. However, it is R4–R6 that should prevent the formation of $ONiO_2$, $NiCO_3$, and $Ni(OH)_2$, and hence a central role in controlling the bottom-side of the Ni layer.

The first objective of the present study was to measure the rate coefficients for R4–R6 and then to insert into a global chemistry-climate model the complete set of Ni reaction kinetics and the experimentally derived MIF for Ni. The purpose of this was to investigate the widely differing lidar measurements of the Ni layer and to understand why the Ni layer profile is broader than Fe on the bottom-side.

2. Underpinning Laboratory and Theoretical Work

2.1. Experimental Method

Reactions R4–R6 were studied in a stainless steel fast flow tube, which has been described in detail previously (Daly et al., 2019; Gómez Martín et al., 2017; Self & Plane, 2003). At the upstream end of the tube, a Nd:YAG laser (Continuum Minilite) was used to ablate Ni atoms from a Ni rod (99.99% purity, Alfa Aesar); each pulse was then entrained in a carrier gas flow of N_2 (99.9999%, Air products, mass flow rate typically 3.3 standard liters per minute). O_3 or O_2 (99.999%, Air products) were added at a fixed injection point 7 cm downstream of the rod to produce NiO or NiO_2, respectively. Atomic O or CO (99.5%, Argo International) were then added via a sliding injector positioned 0.5 cm upstream of the O_3 and O_2 injection point. At the end of the flow tube, after a reaction time of several milliseconds, Ni atoms were probed by LIF at 341.476 nm [Ni($z^3F_4^0$-a^3D_3)]. An Edwards E2M80 pump with a roots blower (Edwards EH500A) was used to provide flow velocities ranging from 48–76 m s^{-1}; at the constant pressure of 1.0 Torr used in all the experiments, this produced reaction times after injection of O or CO of 3.5–5.0 ms. All of the experiments reported in this study were conducted at 294 K.

O_3 was generated by flowing O_2 through a high voltage corona in a commercial ozonizer, and its concentration measured spectrophotometrically at 253.7 nm (provided by a Hg pen lamp) in a 19 cm path length optical cell. The O_3 absorption cross section was taken as 1.16×10^{-17} cm^2 (Molina & Molina, 1986). Atomic O was generated by the microwave discharge of N_2 (McCarroll cavity, Opthos Instruments Inc.), followed by titration with NO (99.95% Air products, purified further via three freeze-pump-thaw cycles) before injection into the flow tube through the sliding injector (Self & Plane, 2003). The concentration of O was determined by using a mass spectrometer (Hiden HPR60) at the downstream end of the flow tube to determine the amount of NO required to titrate the O. The (first-order) loss rate of O to the walls of the flow tube was measured from the relative change in [O] as the carrier gas flow rate, and therefore the flight time, was varied at constant pressure. The change in [O] was monitored by adding NO downstream and measuring the relative intensity of the chemiluminescence (at $\lambda > 550$ nm) produced by the reaction between NO and O (Self & Plane, 2003).

2.2. Experimental Results

The kinetics in the flow tube are complex, involving several gas-phase reactions and diffusional loss to the walls. A kinetic model of the flow tube was therefore used to optimize each rate coefficient of interest (i.e., k_4, k_5, or k_6). The time-dependent variation of the Ni species and O were described by a set of Ordinary Differential Equations (ODEs). Full details of the model are given elsewhere (Bones et al., 2020). The value and uncertainty of each rate coefficient under study was determined by doing an independent fit to each experimental data point and then calculating the mean and standard deviation. The (first-order) wall loss rate of Ni was measured to be 150 ± 22 s^{-1}. For NiO and NiO_2, a loss rate of 130 s^{-1} was estimated from the long-range capture forces between these oxides and N_2, a method we have described elsewhere (Self
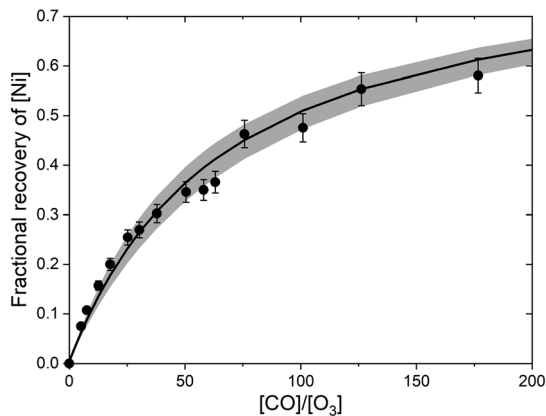
Figure 2. A plot of the fractional recovery in [Ni] (where 0 is the Ni concentration when [CO] = 0) as a function of [CO]/[O$_3$], where [O$_3$] is fixed at 1.8×10^{12} cm^{-3}. The solid black points are the experimental data and the solid black line is the model fit with $\pm 1\sigma$ uncertainty (shaded region). Conditions: 1 Torr, 294 K.
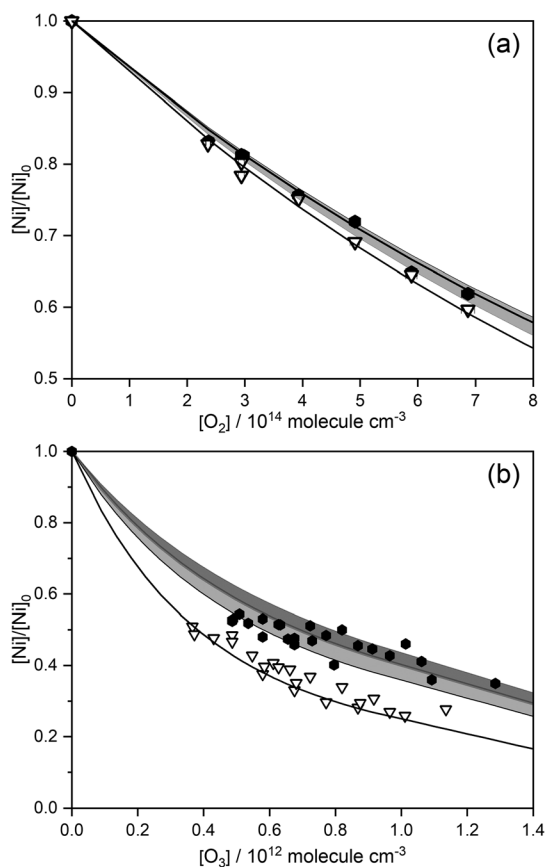
Figure 3. (a) Plots of [Ni]/[Ni]$_0$ as a function of [O$_2$]. (b) Plots of [Ni]/[Ni]$_0$ as a function of [O$_3$]. Experimental data: Solid black circles are experimental data for the fixed addition of O ([O] = 9.2×10^{12} molecule cm^{-3} at the point of injection); open triangles are without O. The solid black lines are the model fits through each dataset. The shaded area of the model fit represents the $\pm 1\sigma$ uncertainty. Conditions: 1 Torr, 294 K.

& Plane, 2003). The atomic O wall loss rate was measured to be 231 ± 31 s^{-1}. Because R5 is simpler to study since it does not involve the generation of O with its attendant wall losses, we describe the measurement of k_5 first.

2.2.1. Reaction of NiO With CO

NiO was produced by R1 through addition of O$_3$ at a point 7 cm downstream of the Ni rod. CO was added 0.5 cm upstream of the O$_3$ injection point via the sliding injector. This gave a reaction time of 5 ms from the sliding injector to the LIF detection point. k_5 was determined by varying [CO] at fixed [O$_3$], and observing the fractional recovery in [Ni] (where 0 is the Ni signal when [CO] = 0). The experimental points are shown in Figure 2. The recycling of Ni was modeled by applying the rate coefficients and branching ratios for Ni and NiO reacting with O$_2$ and O$_3$ (i.e., R1, R2, R3a, and R3b) determined previously (Mangan et al., 2019). A satisfactory fit of the model to the experimental data is obtained with k_5(294 K) = $(3.0 \pm 0.5) \times 10^{-11}$ cm^3 molecule^{-1} s^{-1}, illustrated in Figure 2. This value is in very good agreement with the only previous study of R5 by Mangan et al. (2019) using the pulsed laser photolysis-laser induced fluorescence (PLP-LIF) technique in a slow flow reactor, which reported k_5(190–377 K) = $(3.2 \pm 0.6) \times 10^{-11}$ $(T/200)^{-0.19 \pm 0.05}$ cm^3 molecule^{-1} s^{-1}, that is, k_5(294 K) = $(3.0 \pm 0.6) \times 10^{-11}$ cm^3 molecule^{-1} s^{-1}.

2.2.2. Reactions of NiO and NiO$_2$ With O

These reactions were studied by injecting a constant concentration of O into the flow tube, and then either adding O$_3$ to produce NiO via R1, or adding O$_2$ to make NiO$_2$ via R2. Since NiO$_2$ is also made via the reaction of NiO with O$_3$, k_6(NiO$_2$ + O) was required for the flow tube model in order to fit k_4(NiO + O); hence, R6 was studied first. Figure 3a shows the [Ni]/[Ni]$_0$ ratio (where 1 is the ratio when [O$_2$] = 0) measured as a function of [O$_2$] (varied from $(2–7) \times 10^{14}$ molecule cm^{-3}), with [O] either set to 0 or a fixed value of 9.2×10^{12} molecule cm^{-3} at the point of injection. Because the O$_3$ was added through a side port of the tube, a mixing time of 1.5 ms was applied in the model. This was estimated as the time taken for O$_3$ to diffuse 1 cm across the tube with D(O$_3$-N$_2$ = 134 cm^2 s^{-1}) at 1 Torr (Langenberg et al., 2020). The model fit through the experimental points yields k_6(294 K) = $(2.5 \pm 1.2) \times 10^{-11}$ cm^{-3} molecule s^{-1}. Figure 3b shows the [Ni]/[Ni]$_0$ ratio as a function of [O$_3$] (varied from $(0.3–1.3) \times 10^{12}$ molecule cm^{-3} with an error of approximately $\pm 10\%$), with [O] again fixed at 9.2×10^{12} molecule cm^{-3}. The model fit yields k_4(294 K) = $(4.6 \pm 1.4) \times 10^{-11}$ cm^3 molecule^{-1} s^{-1}. Because [O] is limited by the microwave discharge efficiency, the wall loss rate of O is of a similar magnitude to the rate of R4. Hence, the modeled fit for k_4 is somewhat sensitive to the atomic O wall loss rate, for example, a 20% change in the O wall loss rate results in a 12% change in the fitted rate coefficient.

2.3. Photochemistry of NiOH

Our previous work on the mesospheric Fe layer showed that FeOH is a major Fe reservoir on the bottom-side of the Fe layer (Feng et al., 2013). However, this hydroxide photolyses relatively rapidly with J(FeOH) = $(6 \pm 3) \times 10^{-3}$ s^{-1} (Viehl et al., 2016). We therefore apply the same quantum chemistry method as in that study to determine J(NiOH). The geometry of NiOH was first optimized at the B3LYP/6-311 + g(2d,p) level of theory using the Gaussian 16 suite of programs (Frisch et al., 2016). The vertical excitation energies and transition
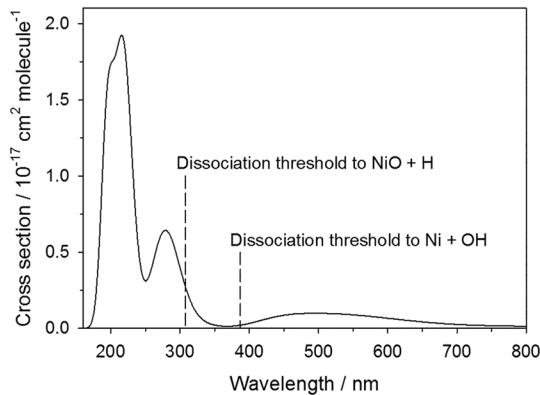
Figure 4. Absorption spectrum of NiOH calculated using time-dependent density function theory at the B3LYP/6-311 + g(2d,p) level of theory (Frisch et al., 2016). The dissociation thresholds to Ni + OH and NiO + H are indicated with dashed lines.

dipole moments for transitions from the ground state to the first 50 electronically excited states were then calculated using time-dependent density function theory (TD-DFT) (Bauernschmitt & Ahlrichs, 1996). The resulting absorption spectrum is plotted in Figure 4. This diagram also shows the dissociation thresholds for the two channels, indicating that photolysis to Ni + OH can occur at wavelengths shorter than 387 nm. Assuming that photolysis starts at this threshold (as appears to be the case for FeOH (Viehl et al., 2016)), then $J(NiOH) = 0.02 \text{ s}^{-1}$ in the MLT (using the solar actinic flux from the semiempirical SOLAR2000 model (Tobiska et al., 2000), averaged over a solar cycle).

3. Atmospheric Modeling

3.1. A Ni Chemistry Scheme for Atmospheric Modeling

The rate coefficients of the neutral and ion-molecule reactions for Ni shown schematically in Figure 1 are listed in Table 1. As indicated by the footnotes to the Table, many of these reactions have now been studied in the laboratory. Where measurements are not available, we have set the rate coefficients to those for the analogous reactions of Fe. This is of course somewhat arbitrary. However, the important Ni reactions that we have set to their Fe analogs are all quite exothermic, and the Fe reactions are already relatively fast. These are reactions R10, R13, R16, R17, R36, and R42.

Reactions R18–R20 in Table 1 are polymerization reactions, which describe the permanent loss of the significant neutral reservoir species NiOH, $Ni(OH)_2$, and $NiCO_3$ to form meteoric smoke particles. We have used this type of reaction previously for modeling the Fe, Mg, Na, K, and Ca layers (Feng et al., 2013; Langowski et al., 2015; Marsh et al., 2013; Plane et al., 2014, 2018). Here, the rate coefficients k_{18-20} are set to $7 \times 10^{-8} \text{ cm}^3 \text{ s}^{-1}$, which is around 80 times larger than a typical dipole–dipole capture rate for these metallic molecules. This factor allows for Ni reservoir species polymerizing with other metal-containing molecules of meteoric origin (e.g., FeOH, $Mg(OH)_2$, and $NaHCO_3$), whose concentration will be around 80 times higher because the elemental ablation ratio of Ni atoms to the sum of Na, Fe, Mg, Si, Al, and K atoms is ~1/80 (Carrillo-Sánchez et al., 2020). For comparison, in the case of two other minor meteoric metals, Ca and K, the dipole-dipole capture rate was increased by factors of 100 (Plane et al., 2018) and 270 (Plane et al., 2014), respectively.

3.2. Whole Atmosphere Model of Ni

The set of Ni reactions in Table 1 was then added into the Whole Atmosphere Community Climate Model (WACCM6), which uses the framework developed from the fully coupled Community Earth System Model (CESM) (Gettelman et al., 2019). WACCM6 extends vertically from the Earth's surface to the lower thermosphere at ~140 km. For this study we used the same horizontal resolution (1.9° latitude × 2.5° longitude) and 88 vertical model layers (height resolution ~3.5 km in the MLT) as in our earlier work on global meteoric metals (Plane et al., 2015), which used WACCM4 in CESM1 (Hurrell et al., 2013). This version of WACCM6 with Ni chemistry is termed WACCM-Ni. The data presented here used a specific dynamics (SD) version of WACCM (Feng et al., 2013; Plane et al., 2018), nudged with NASA's Modern-Era Retrospective Analysis for Research and Applications (MERRA2) (Molod et al., 2015). To allow comparison of Ni and Ni^+ with Fe and Fe^+, which are much better characterized through observations in the MLT, the full set of Fe reactions in WACCM-Fe (Bones et al., 2016; Feng et al., 2013; Viehl et al., 2016) was included.

The global average injection profiles of Ni and Fe are shown in Figure 5. These are the profiles predicted by the CABMOD-ZoDy model (Carrillo-Sánchez et al., 2020) described in section 1. Both profiles were initially reduced by a factor of 5, following our previous work (Plane et al., 2018). This factor compensates for the fact that global models such as WACCM underestimate the vertical transport of minor species in the MLT, because short wavelength gravity waves are not resolved on the model horizontal grid scale (~150 km). These subgrid waves contribute to chemical and dynamical transport while dissipating, and this can exceed transport driven along mixing ratio gradients by the turbulent eddy diffusion produced once the waves break

Table 1
Ni Chemistry in the MLT

No.	Reaction	Rate coefficient[a]
Neutral reactions		
R1	$Ni + O_3 \rightarrow NiO + O_2$	$k_1 = 6.5 \times 10^{-10}(T/293)^{0.167}$ [b]
R2	$Ni + O_2 (+M) \rightarrow NiO_2$	$\log_{10}(k_2) = -37.592 + 7.168\log_{10}(T) - 1.565(\log_{10}(T))^2$ [b]
R3a	$NiO + O_3 \rightarrow NiO_2 + O_2$	$k_{3a} = 2.5 \times 10^{-10}(T/293)^{0.167}$ [b]
R3b	$NiO + O_3 \rightarrow Ni + 2O_2$	$k_{3b} = 1.4 \times 10^{-10}(T/293)^{0.167}$ [b]
R4	$NiO + O \rightarrow Ni + O_2$	$k_4 = 1.5 \times 10^{-10} \exp(-337/T)$ [c]
R5	$NiO + CO \rightarrow Ni + CO_2$	$k_5 = 3.2 \times 10^{-11}(T/200)^{-0.194}$ [b,c]
R6	$NiO_2 + O \rightarrow NiO + O_2$	$k_6 = 7.9 \times 10^{-11} \exp(-337/T)$ [c]
R7	$NiO + O_2 (+M) \rightarrow ONiO_2$	$\log_{10}(k_7) = -41.0913 + 10.1064\log_{10}(T) - 2.2610(\log_{10}(T))^2$ [b]
R8	$NiO + CO_2 (+M) \rightarrow NiCO_3$	$\log_{10}(k_8) = -41.4265 + 10.9640\log_{10}(T) - 2.5287(\log_{10}(T))^2$ [b]
R9	$NiO + H_2O (+M) \rightarrow Ni(OH)_2$	$\log_{10}(k_9) = -29.7651 + 5.2064\log_{10}(T) - 1.7118(\log_{10}(T))^2$ [b]
R10	$NiO_2 + O_3 \rightarrow ONiO_2 + O_2$	$k_{10} = 3.4 \times 10^{-10} \exp(-337/T)$ [d]
R11	$ONiO_2 + O \rightarrow NiO_2 + O_2$	$k_{11} = 2.3 \times 10^{-10} \exp(-2,310/T)$ [d]
R12	$NiCO_3 + O \rightarrow NiO_2 + CO_2$	$k_{12} = 2.3 \times 10^{-10} \exp(-2,310/T)$ [d]
R13	$ONiO_2 + H_2O \rightarrow Ni(OH)_2 + O_2$	$k_{13} = 5 \times 10^{-12}$ [d]
R14	$Ni(OH)_2 + H \rightarrow NiOH + H_2O$	$k_{14} = 3 \times 10^{-10} \exp(-796/T)$ [d]
R15	$NiCO_3 + H \rightarrow NiOH + CO_2$	$k_{15} = 3 \times 10^{-10} \exp(-796/T)$ [d]
R16	$ONiO_2 + H \rightarrow NiOH + O_2$	$k_{16} = 3 \times 10^{-10} \exp(-302/T)$ [d]
R17	$NiOH + H \rightarrow Ni + H_2O$	$k_{17} = 5 \times 10^{-11} \exp(-337/T)$ [d]
R18	$NiOH + NiOH \rightarrow (NiOH)_2$	$k_{18} = 7 \times 10^{-8}$ [e]
R19	$Ni(OH)_2 + Ni(OH)_2 \rightarrow (Ni(OH)_2)_2$	$k_{19} = 7 \times 10^{-8}$ [e]
R20	$NiCO_3 + NiCO_3 \rightarrow (NiCO_3)_2$	$k_{20} = 7 \times 10^{-8}$ [e]
R21	$NiOH + h\nu \rightarrow Ni + OH$	$k_{21} = 1.8 \times 10^{-2}$ [f]
Ion-molecule reactions		
R22	$Ni^+ + O_3 \rightarrow NiO^+ + O_2$	$k_{22} = 9.8 \times 10^{-10}(T/294)^{-0.16}$ [g]
R23	$Ni^+ + N_2 (+M) \rightarrow Ni^+.N_2$	$\log_{10}(k_{23}) = -27.5009 + 1.0667\log_{10}(T) - 0.74741(\log_{10}(T))^2$ [g]
R24	$Ni^+ + O_2 (+M) \rightarrow NiO_2^+$	$\log_{10}(k_{24}) = -27.8098 + 1.3065\log_{10}(T) - 0.81136(\log_{10}(T))^2$ [g]
R25	$Ni^+ + CO_2 (+M) \rightarrow Ni^+.CO_2$	$\log_{10}(k_{25}) = -29.805 + 4.2282\log_{10}(T) - 1.4303(\log_{10}(T))^2$ [g]
R26	$Ni^+ + H_2O (+M) \rightarrow Ni^+.H_2O$	$\log_{10}(k_{26}) = -24.318 + 0.20448\log_{10}(T) - 0.66676(\log_{10}(T))^2$ [g]
R27	$NiO^+ + O \rightarrow Ni^+ + O_2$	$k_{27} = 1.7 \times 10^{-10}$ [g]
R28	$NiO^+ + CO \rightarrow Ni^+ + CO_2$	$k_{28} = 7.4 \times 10^{-11}$ [g]
R29a	$NiO^+ + O_3 \rightarrow Ni^+ + 2O_2$	$k_{29a} = 7.8 \times 10^{-11}$ [g]
R29b	$NiO^+ + O_3 \rightarrow NiO_2^+ + O_2$	$k_{29b} = 1.9 \times 10^{-10}$ [g]
R30	$NiO_2^+ + O_3 \rightarrow NiO^+ + 2O_2$	$k_{30} = 4.6 \times 10^{-11}$ [g]
R31	$Ni^+.N_2 + O \rightarrow NiO^+ + N_2$	$k_{31} = 7 \times 10^{-12}$ [g]
R32	$NiO_2^+ + O \rightarrow NiO^+ + O_2$	$k_{32} = 5 \times 10^{-11}$ [d]
R33	$Ni^+.CO_2 + O \rightarrow NiO^+ + CO_2$	$k_{33} = 2 \times 10^{-10}$ [d]
R34	$Ni^+.H_2O + O \rightarrow NiO^+ + H_2O$	$k_{34} = 2 \times 10^{-10}$ [d]
R35	$Ni^+ + e^- \rightarrow Ni + h\nu$	$k_{35} = 8 \times 10^{-12}(T/300)^{-0.51}$ [d]
R36	$NiO^+ + e^- \rightarrow Ni + O$	$k_{36} = 5.5 \times 10^{-7}(300/T)^{0.5}$ [d]
R37	$NiO_2^+ + e^- \rightarrow Ni + O_2$	$k_{37} = 3 \times 10^{-7}(T/200)^{-0.5}$ [d]
R38	$Ni^+.CO_2 + e^- \rightarrow Ni + CO_2$	$k_{38} = 3 \times 10^{-7}(T/200)^{-0.5}$ [d]
R39	$Ni^+.H_2O + e^- \rightarrow Ni + H_2O$	$k_{39} = 3 \times 10^{-7}(T/200)^{-0.5}$ [d]
R40	$Ni^+.N_2 + e^- \rightarrow Ni + N_2$	$k_{40} = 3 \times 10^{-7}(T/200)^{-0.5}$ [d]
R41a	$Ni + O_2^+ \rightarrow Ni^+ + O_2$	$k_{41a} = 3.1 \times 10^{-10}$ [h]
R41b	$Ni + O_2^+ \rightarrow NiO^+ + O$	$k_{41b} = 8.0 \times 10^{-10}$ [h]
R42	$Ni + NO^+ \rightarrow Ni^+ + NO$	$k_{42} = 9.2 \times 10^{-10}$ [d]
R43	$Ni + h\nu \rightarrow Ni^+ + e^-$	$k_{43} = 6.8 \times 10^{-8}$ [i]

[a] Units: s^{-1} for photolysis reactions; cm^3 molecule^{-1} s^{-1} for bimolecular reactions; cm^6 molecule^{-2} s^{-1} for termolecular reactions. [b] Mangan et al. (2019). [c] Measured, this study. [d] Set to the analogous reaction for Fe (Feng et al., 2013) with updated rate coefficients from Plane et al. (2015), Bones et al. (2016), and Viehl et al. (2016). [e] See text. [f] Calculated, this study. [g] Bones et al. (2020). [h] Schlemmer et al. (2003) measured the reaction channel producing $NiO^+ + O$; the channel to $Ni^+ + O_2$ is then set so the overall rate coefficient is at the Langevin capture rate. [i] Photoionization rate at 100 km, using photoionization cross sections from Heays et al. (2017).
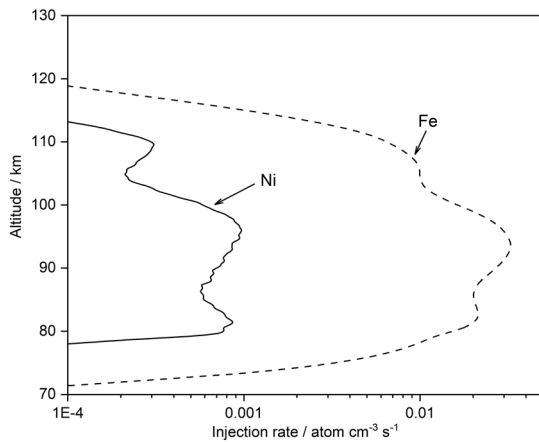
Figure 5. Global annual mean injection rates of Ni and Fe resulting from meteoric ablation. The injection profiles from Carrillo-Sánchez et al. (2020) have been divided by factors of 10.5 and 5.0 for Ni and Fe, respectively (see text for further details).

(Gardner et al., 2016). Because these additional vertical transport mechanisms are underestimated, the MIF needs to be reduced in order to simulate the observed metal density (Plane et al., 2018).

In CABMOD-3, cosmic dust particles are set to have a 90 wt% $Fe-Mg-SiO_4$ phase and a 10 wt% metallic Fe-Ni phase, so that ~70% of the total Fe is embedded inside the silicate bulk (Bones et al., 2019; Carrillo-Sánchez et al., 2020). The elemental Fe:Ni ratio in the metallic phase is then set to 5.5, so that the overall Fe:Ni abundance ratio in the particle is the CI ratio of 18:1 (Asplund et al., 2009). Our approach in the present study was to scale the Ni MIF to optimize the WACCM-Ni simulated layer to the measured Ni layer. For the Chatanika measurements (Collins et al., 2015) this required the Ni MIF to be increased, relative to Fe, by a factor of 15 compared to the CI ratio (Carrillo-Sánchez et al., 2020). This degree of Ni enrichment seems extremely unlikely. In contrast, the Kühlungsborn measurements (Gerding et al., 2019) require the Ni MIF to be decreased by a factor of only 2.1 relative to the Fe MIF—which would be explained if the Fe:Ni ratio in the metallic phase was ~12, or the Fe-Ni phase was ~5 wt% of the cosmic dust particles. Interestingly, a similar discrepancy was found between $Fe^+:Ni^+$ measurements in the Martian thermosphere and the CABMOD-ZoDy prediction (Carrillo-Sánchez et al., 2020). In any case, the relative Ni MIF will be refined further once more lidar measurements become available. The seasonal and geographical variation of the Ni MIF was then scaled to the variation in the Fe MIF determined previously using an astronomical dust model (Feng et al., 2013; Fentzke & Janches, 2008).

After determining the optimal Ni MIF during 2 years of model spin up, WACCM-Ni was run for a full year simulation from January to December 2012. Although the Ni observations of Gerding et al. (2019) were performed in early 2018, some input files (solar input, CMIP6 emissions, and chemical species at the surface) in the released CESM2_1_1 are not yet available from 2015 onward. We therefore chose 2012 as the most recent year in which there were no major perturbations during the observational period (January–March), such as the major sudden stratospheric warming in January 2013 (Manney et al., 2015), which would have perturbed the Ni abundance in the model (Feng et al., 2017). Although the choice of 2012 is somewhat arbitrary, the aim here is to present the first atmospheric model of Ni and compare to the very limited observational data sets currently available.

3.3. Observational Data

The Ni layer measurements of Collins et al. (2015) require an extremely large Ni enrichment in cosmic dust (section 3.2). Moreover, because the measured $Fe^+:Ni^+$ ratio in the MLT is ~20:1 (Carrillo-Sánchez et al., 2020), the neutral ratio cannot be explained by most of the nickel being partitioned into Ni rather than Ni^+. We therefore focus on the Kühlungsborn observations, recorded between January and March 2018 (Gerding et al., 2019). The data from five nights, measured with the stronger $Ni(a^3D_3-^3F_4)$ transition at 341.48 nm, were averaged to provide a single profile. For comparison with the Fe layer, we use lidar observations from Urbana-Champaign (40°N, 272°E) between October 1989 and June 1992 (Feng et al., 2013; Helmer et al., 1998). This is another midlatitude location with a large set of Fe lidar measurements. Data for the late winter period (January–March) from 3 years was averaged, which should remove some interannual variability. Rocket-borne mass spectrometric measurements of Ni^+ ($m/z = 58$) and Fe^+ ($m/z = 56$) density profiles (including a correction for their isotopic abundances) were taken from eight of the nine flights detailed in Gómez Martín et al. (2017); Flight S37/P was excluded because of poor data quality. A geometric mean and standard deviation from these flights was determined for comparison with the Ni^+ and Fe^+ model output.

3.4. Mean Profiles of Ni and Ni^+ Simulated by WACCM-Ni

Figure 6 illustrates the profiles of the Ni species around midnight, averaged over the same period (January−March) as the observations (Gerding et al., 2019). This shows very satisfactory agreement between the mean lidar profile and simulated Ni layer, with both peaking at 86 km with a peak
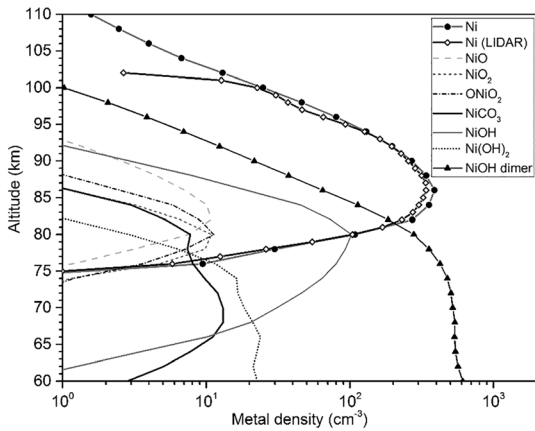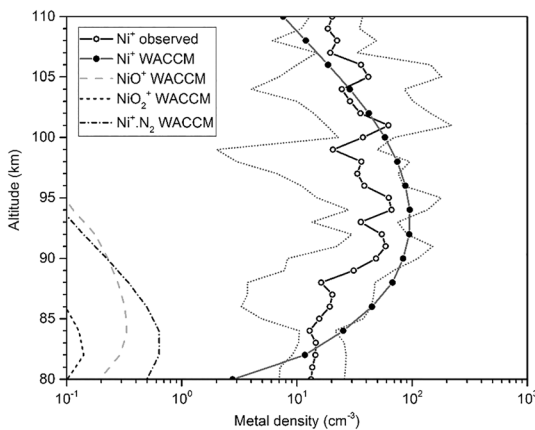
Figure 6. Mean altitude profiles at midnight of Ni species simulated by WACCM-Ni and Ni lidar observations, between January and March at Kühlungsborn (54°N, 12°E).

density of 350 cm^{-3}, and similar top-side and bottom-side scale heights. Of course, the absolute concentration is fitted by varying the Fe:Ni ratio in the metallic phase in CABMOD-3 (section 3.2). However, the layer peak height and the scale heights are a good test of the neutral and ion-molecule chemistry. Figure 6 also shows that the major neutral reservoirs are the hydroxides NiOH and Ni(OH)$_2$, and the sink for Ni is the (NiOH)$_2$ dimer which plays the role of a surrogate for meteoric smoke. The oxides (NiO, NiO$_2$, and ONiO$_2$) appear in relatively narrow layers peaking between 78 and 83 km, with peak concentrations of only ~10 cm^{-3}, because they are converted to the more stable hydroxides by reaction of NiO with H$_2$O (R9) (Mangan et al., 2019), and ONiO$_2$ with H and H$_2$O (R13 and R16) based on the analogous chemistry of Fe and Ca (Plane et al., 2015, 2018). NiCO$_3$ is also a minor reservoir because it is converted to NiOH by reaction with H (R15).

Figure 7 compares the vertical mean Ni$^+$ profile simulated by WACCM-Ni with the mean profile from the sounding rockets. The modeled profile agrees reasonably well, within the 1σ envelope of the rocket average. The modeled Ni$^+$ layer peaks around 94 km with a peak density of 95 cm^{-3}, compared with the observed peak of 70 cm^{-3}. The modeled column abundance between 80 and 110 km is 1.5×10^8 cm^{-2}, compared with a measured abundance of 9.7×10^7 cm^{-2}. The molecular ions NiO$^+$, NiO$_2{}^+$, and Ni$^+$.N$_2$ are predicted to have much lower concentrations (<1 cm^{-3}).

3.5. Diurnal Variation of Ni and Ni$^+$ Simulated by WACCM-Ni

Figure 8 contains altitude-time plots of the Ni and Ni$^+$ densities, where the WACCM-Ni output is sampled every hour and averaged over the month of April at Kühlungsborn (54°N, 12°E). In Figure 8a the Ni peak density varies by 15%, with the peak altitude decreasing from 86 km at 00:00 to 84 km at 16:30 hr. Between 04:00 and 19:00 hr there is an increase of Ni on the bottom-side of the layer: the density increases to 150 cm^{-3} at 80 km, and to 0.1 cm^{-3} at 72 km. These changes are caused by photolysis of NiOH (R21), and an increase of atomic O and H, and decrease of O$_3$, during daylight hours (Plane et al., 2015).

The Ni$^+$ layer (Figure 8b) does not exhibit significant diurnal variation on the top-side or bottom-side. However, there is an increase in the Ni$^+$ peak density by a factor of ~2 between night and day (0900–1900 hr), caused by the increase of ambient NO$^+$ and O$_2{}^+$ through photoionization; these ions charge transfer with Ni (R41 and R42). Note that the photoionization of Ni (R43) is not competitive. Another factor is that atomic O increases during daytime through photolysis of O$_2$ and thus more efficiently recycles NiO$^+$ to Ni$^+$ (R27), preventing dissociative recombination with electrons (R36).

3.6. Global Column Abundances of Ni and Fe

Figures 9a and 9b are latitude-month plots showing the seasonal variation of the diurnally averaged Ni and Ni$^+$ column abundances, respectively. The Ni column exhibits a wintertime maximum and summertime minimum. The seasonal variation increases with latitude, and the highest abundance is over Antarctica during winter, which is very likely because of convergence of mesospheric air over the polar vortex (Gardner et al., 2005). This pattern is similar to other meteoric metals such as Fe (Feng et al., 2013), Mg (Langowski et al., 2015), and Na (Marsh et al., 2013). At northern high latitudes, the increase from summer to winter is a factor of ~7 for Ni, close to the approximately sixfold increase observed for the other metals. However, the approximately elevenfold increase in Ni over Antarctica is somewhat more than for these other metals (which exhibit a sixfold to eightfold increase). The column abundances measured at Kühlungsborn ranged from $(3.1–4.9) \times 10^8$ cm^{-2} between January and

Figure 7. Mean altitude profiles at midnight of ionized Ni species simulated by WACCM-Ni between January and March at Kühlungsborn (54°N, 12°E). The solid black line with open circles is the geometric mean profile of Ni$^+$, with the geometric standard deviation (1σ error limits) shown by gray dotted lines, for the eight rocket flights described in Gómez Martín et al. (2017).
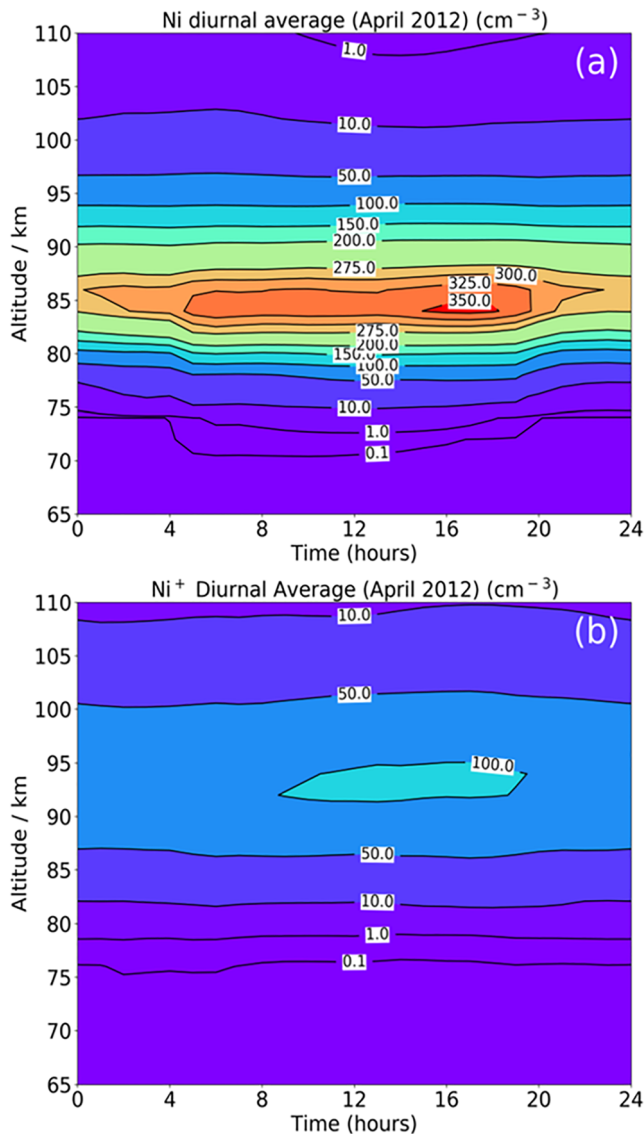
Figure 8. Altitude-time plots of the hourly average profiles of the (a) Ni and (b) Ni^+ densities (in cm^{-3}), simulated by WACCM-Ni for April at 54°N, 12°E (Kühlungsborn).

March (Gerding et al., 2019), which compares well with the WACCM-Ni column abundance of $(4.5 \pm 1.5) \times 10^8 \ cm^{-2}$ averaged over the same period and location.

The modeled Ni^+ layer column abundance in Figure 9b exhibits much less seasonal variation than Ni. The modeled global seasonal Ni^+:Ni average is 0.34. This is a lower ratio than both the modeled Fe^+:Fe (Feng et al., 2013) and Na^+:Na (Marsh et al., 2013) ratios, which have seasonal averages close to unity, and much lower than the modeled Ca^+:Ca seasonal average of 11, which is caused by the unusually large photoionization rate of Ca and its charge transfer rate with NO^+ (Plane et al., 2018). Interestingly, when compared to rocket-borne observations, the Fe^+:Fe and Na^+:Na ratios are ~0.2 (Feng et al., 2013; Marsh et al., 2013; Plane, 2004), which is a factor of 5 times smaller than modeled by WACCM, and the observed Ca^+:Ca ratio is a factor of ~2 smaller. In contrast, the observed Ni^+:Ni (using the average Ni column abundance from Gerding et al., 2019, of $4.1 \times 10^8 \ cm^{-2}$) is 0.24, which is only 29% smaller than the modeled ratio.

Figure 9c illustrates the modeled seasonal variation of the Fe:Ni column abundance ratio as a function of latitude. There is no pronounced trend, other than a decrease in late winter/early spring around 60°S. This seems to be caused by the faster photolysis of NiOH (section 2.3) compared with FeOH (Viehl et al., 2016). The global average modeled Fe:Ni ratio is 36 ± 3, in agreement with the observed ratio of 38 ± 11 (Gerding et al., 2019). In Figure 9d, the Fe^+:Ni^+ ratio does exhibit a seasonal variation with a wintertime minimum, although the absolute variation is small. The mean Fe^+:Ni^+ ratio is 33 ± 1, which is at the upper limit of the ratio of 20^{+13}_{-8} measured by rocket-borne mass spectrometry (Carrillo-Sánchez et al., 2020).

3.7. Comparison of the Ni and Fe Layer Altitude Profiles

Figure 10 compares the neutral profiles of nighttime Ni and Fe at midlatitudes, averaged from January to March. Figure 10a shows lidar measurements of the Fe layer at Urbana-Champaign (40°N; 88°E), and the Ni layer at Kühlungsborn (54°N, 12°E). Figure 10b shows the nighttime layers simulated by WACCM-Ni and WACCM-Fe for the same locations and months. The observations and modeling show that both layers peak at ~86 km. The two lidar studies of the Ni layer (Collins et al., 2015; Gerding et al., 2019) both observed that the bottom-side of the layer is 1–2 km lower than the Fe layer between 78 and 85 km (Figure 10a). This feature is also captured by WACCM (Figure 10b). When comparing the kinetics of the two metals, this is at first glance surprising: the oxidation of Ni by O_3 (R1) is ~2 times faster than Fe, and the reduction of NiO back to Ni by O (R4) is ~3 times slower than the Fe reaction. However, Rollason and Plane (2000) showed that the rate coefficient for the reaction $FeO + O_3 \rightarrow Fe + 2O_2$ is at least one order of magnitude slower than the analogous reaction of NiO (R3b). More important is the reaction of these metal oxides with CO. The reaction FeO + CO is relatively slow, k (FeO + CO, 294 K) $= 1.5 \times 10^{-13} \ cm^{-3}$ (Smirnov, 2008). In contrast, k_5(NiO + CO, 294 K) is ~210 times faster (section 2). Considering that the atomic O density decreases very rapidly below 85 km at night (Plane, 2003), but there is still significant O_3 and CO (primarily due to CO_2 photolysis), the NiO + CO reaction becomes more important below 84 km than NiO + O for recycling NiO to Ni, with NiO + O_3 playing a secondary role (Mangan et al., 2019). These two reactions account for the broader bottom-side of the Ni layer. Note that the observed scale height of the bottom-side of the Ni layer (Figure 10a) is only 1.1 km, compared with 2.9 km for the Fe layer. The respective scale heights from WACCM (Figure 10b) are 1.1 and 3.0 km.
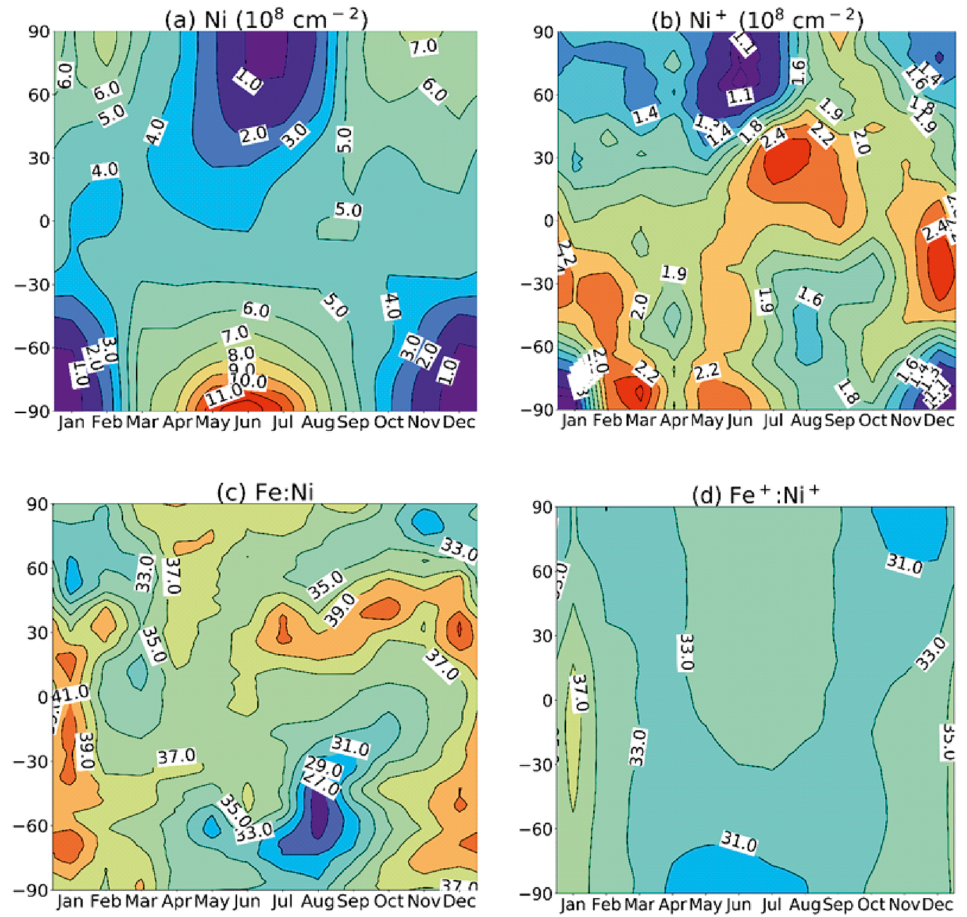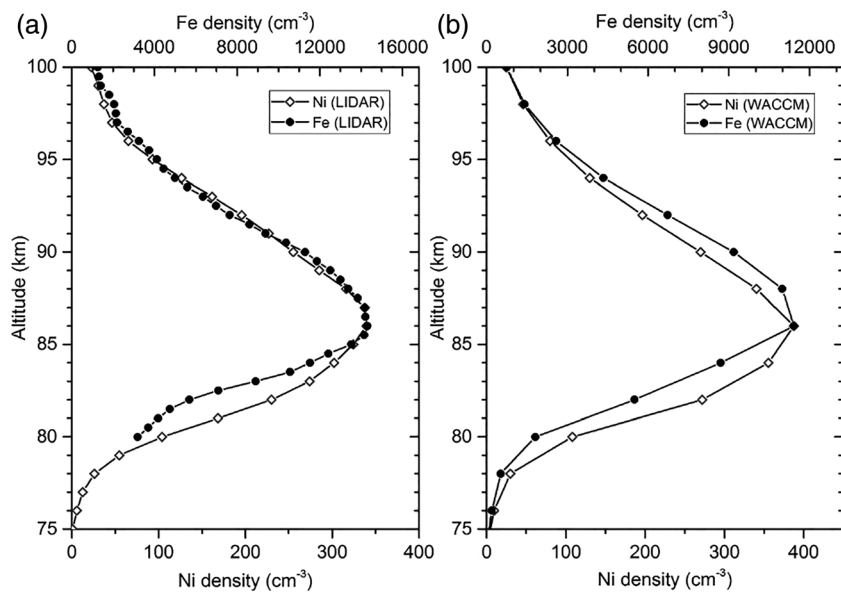
Figure 9. Monthly averaged column abundances as a function of season and month, simulated by WACCM-Ni and WACCM-Fe: (a) Ni, (b) Ni^+, (c) Fe:Ni ratio, and (d) $Fe^+:Ni^+$ ratio. Note that (c) and (d) are plotted with the same contour color scale.

Figure 10. The nighttime average Ni and Fe layers at midlatitudes between January and March: (a) lidar observations; (b) WACCM modeling. The layer peak densities are plotted to overlap by using different scales for Ni density (lower abscissa) and Fe density (upper abscissa).
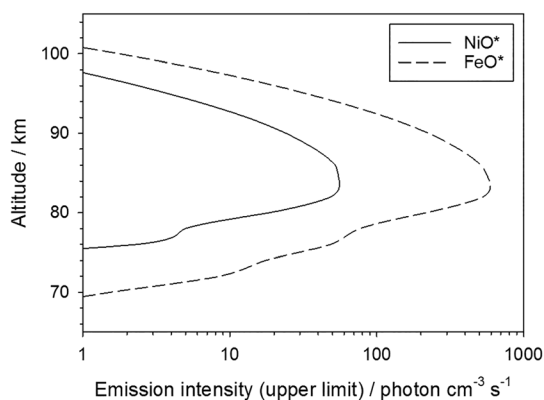
Figure 11. Vertical profiles of NiO* and FeO* chemiluminescence emission rates, assuming a 100% quantum efficiency for the reactions of Ni and Fe with O_3.

3.8. Nightglow Emission From NiO* and FeO*

Electronically excited NiO* can only be produced by the reaction between Ni and O_3 (R1), which is sufficiently exothermic ($\Delta H^o = -297$ kJ mol^{-1}; Mangan et al., 2019) to produce chemiluminescence at wavelengths greater than 402 nm, consistent with the OSIRIS nightglow measurement of an onset at 440 nm (Evans et al., 2011). An upper limit to the nightglow emission rate from NiO* is then given by $k_1[Ni][O_3]$, which assumes that a photon is produced from every time Ni and O_3 react, that is, a quantum yield (QY) of 1. Figure 11 shows the calculated NiO* emission profile for midlatitudes between January and March. Also shown is the FeO* emission profile calculated from the WACCM-Fe output (note that the altitude of peak FeO* emission was previously calculated to be ~4 km higher using a 1-D model (Saran et al., 2011), though that model also placed the Fe layer peak 3 km higher than observed). The integrated emission intensities from the NiO* and FeO* layers in Figure 11 are then 54 and 559 R, respectively. If both reactions have a similar QY, then this would give NiO*/FeO* = 0.10. Evans et al. (2011) reported that the NiO*/FeO* ratio retrieved from OSIRIS limb spectra ranged from 0.05 to 0.3, which brackets the model estimate and therefore implies that the QYs are similar. The most recent estimate for QY(FeO*) is $(13 \pm 3)\%$ (Unterguggenberger et al., 2017), indicating that QY(NiO*) lies between 6% and 40%.

Figure 11 shows that the FeO* layer peaks at 84 km, in excellent agreement with OSIRIS observations (Evans et al., 2011). WACCM-Ni predicts that the NiO* layer should also peak at 84 km (Figure 11). Although the satellite limb observations indicate the peak may be slightly higher (86–89 km) (Evans et al., 2011), the NiO* emission signal is noisy because it is weak and overlain by FeO*, Na D, OH Meinel, O_2 Herzberg and NO_2 emissions.

4. Conclusions

This study describes the development of the first model of meteoric Ni in the MLT. Building on previous work on the kinetics of neutral and ion-molecule reactions of Ni-containing species, we describe here a set of underpinning experimental and theoretical work on the reactions of NiO with O and CO, NiO_2 with O, and the photolysis of NiOH. A WACCM-Ni simulation with specified dynamics is then presented. Good agreement is achieved between the modeled layer and a limited set of lidar observations of the Ni layer at a midlatitude site (Kühlungsborn, 54°N), if the Ni meteoric input function is reduced by a factor of 2.1 compared with Fe. The modeled Fe:Ni column abundance ratio in the MLT of 36 ± 3 is then close to the observed ratio at midlatitudes. The modeled Ni^+ peak density is slightly overestimated—though within a standard deviation—of the geometric mean of a small number of rocket-borne measurements. The broader bottom-side of the Ni layer, compared with Fe, appears to be explained by the faster Ni recycling reactions of NiO with CO and O_3. Lastly, the quantum yield for photon production from the reaction between Ni and O_3, which contributes to the nightglow, is relatively large and similar to that for the Fe analog.

Future improvements to the Ni model—for example, refining the rate coefficients of the small number of reactions which are currently set to be the same as their Fe analogs, and optimizing the relative meteoric input of Ni to Fe—will require more comprehensive lidar observations of the Ni layer at different latitudes and seasons.

Conflict of Interest

There are no financial or other conflicts of interest for any author.

Data Availability Statement

The rocket flight data were kindly provided by E. Kopp (University of Bern). The CESM2 model is available at https://github.com/ESCOMP/CESM.git and the MERRA2 reanalysis data set is available at NCAR research archive (https://rda.ucar.edu/data/ds313.3/). The new version of CESM2 with the Ni and Fe

codes and model output, as well as the data used in the paper, is archived at the Leeds University PetaByte Environmental Tape Archive and Library (PETAL; https://petal.leeds.ac.uk/). The data can be downloaded online (https://doi.org/10.5281/zenodo.3872990).

References

Arndt, P., Bohsung, J., Maetz, M., & Jessberger, E. K. (1996). The elemental abundances in interplanetary dust particles. *Meteoritics and Planetary Science*, *31*(6), 817–833. https://doi.org/10.1111/j.1945-5100.1996.tb02116.x

Asplund, M., Grevesse, N., Sauval, A. J., & Scott, P. (2009). The chemical composition of the Sun. In R. Blandford, J. Kormendy, & E. van Dishoeck (Eds.), *Ann. Rev. Astron. Astrophys* (Vol. 47, pp. 481–522). Palo Alto: Annual Reviews. https://doi.org/10.1146/annurev.astro.46.060407.145222

Bauernschmitt, R., & Ahlrichs, R. (1996). Treatment of electronic excitations within the adiabatic approximation of time dependent density functional theory. *Chemical Physics Letters*, *256*(4-5), 454–464. https://doi.org/10.1016/0009-2614(96)00440-X

Bills, R. E., & Gardner, C. S. (1990). Lidar observations of mesospheric Fe and sporadic Fe layers at Urbana, Illinois. *Geophysical Research Letters*, *17*(2), 143–146. https://doi.org/10.1029/GL017i002p00143

Bones, D. L., Carrillo-Sánchez, J. D., Kulak, A. N., & Plane, J. M. C. (2019). Ablation of Ni from micrometeoroids in the upper atmosphere: Experimental and computer simulations and implications for Fe ablation. *Planetary and Space Science*, *179*, 104725.

Bones, D. L., Daly, S., Mangan, T. P., & Plane, J. M. C. (2020). A study of the reactions of Ni^+ and NiO^+ ions relevant to planetary upper atmospheres. *Physical Chemistry Chemical Physics*, *22*, 8940–8951. https://doi.org/10.1039/D1030CP01124J

Bones, D. L., Plane, J. M. C., & Feng, W. (2016). Dissociative recombination of FeO^+ with electrons: Implications for plasma layers in the ionosphere. *The Journal of Physical Chemistry. A*, *120*(9), 1369–1376. https://doi.org/10.1021/acs.jpca.5b04947

Broadfoot, A. L., & Bellaire, P. J. Jr. (1999). Bridging the gap between ground-based and space-based observations of the night airglow. *Journal of Geophysical Research*, *104*(A8), 17,127–17,138. https://doi.org/10.1029/1999JA900135

Carrillo-Sánchez, J. D., Gómez-Martín, J. C., Bones, D. L., Nesvorný, D., Pokorný, P., Benna, M., et al. (2020). Cosmic dust fluxes in the atmospheres of Earth, Mars, and Venus. *Icarus*, *335*, 113395. https://doi.org/10.1016/j.icarus.2019.113395

Collins, R. L., Li, J., & Martus, C. M. (2015). First lidar observation of the mesospheric nickel layer. *Geophysical Research Letters*, *42*, 665–671. https://doi.org/10.1002/2014GL062716

Daly, S. M., Bones, D. L., & Plane, J. M. C. (2019). A study of the reactions of Al^+ ions with O_3, N_2, O_2, CO_2 and H_2O: Influence on Al^+ chemistry in planetary ionospheres. *Physical Chemistry Chemical Physics*, *21*(26), 14,080–14,089. https://doi.org/10.1039/C8CP07572G

Evans, W. F. J., Gattinger, R. L., Broadfoot, A. L., & Llewellyn, E. J. (2011). The observation of chemiluminescent NiO* emissions in the laboratory and in the night airglow. *Atmospheric Chemistry and Physics*, *11*(18), 9595–9603. https://doi.org/10.5194/acp-11-9595-2011

Feng, W., Kaifler, B., Marsh, D. R., Höffner, J., Hoppe, U.-P., Williams, B. P., & Plane, J. M. C. (2017). Impacts of a sudden stratospheric warming on the mesospheric metal layers. *Journal of Atmospheric and Solar - Terrestrial Physics*, *162*, 162–171. https://doi.org/10.1016/j.jastp.2017.02.004

Feng, W., Marsh, D. R., Chipperfield, M. P., Janches, D., Höffner, J., Yi, F., & Plane, J. M. C. (2013). A global atmospheric model of meteoric iron. *Journal of Geophysical Research: Atmospheres*, *118*, 9456–9474. https://doi.org/10.1002/jgrd.50708

Fentzke, J. T., & Janches, D. (2008). A semi-empirical model of the contribution from sporadic meteoroid sources on the meteor input function in the MLT observed at Arecibo. *Journal of Geophysical Research*, *113*, A03304. https://doi.org/10.1029/2007JA012531

Frisch, M. J., Trucks, G. W., Schlegel, H. B., Scuseria, G. E., Robb, M. A., Cheeseman, J. R., et al. (2016). *Gaussian 16, revision B.01*. Wallingford, CT: Gaussian, Inc.

Gardner, C. S., Liu, A. Z., & Guo, Y. (2016). Vertical and horizontal transport of mesospheric Na: Implications for the mass influx of cosmic dust. *Journal of Atmospheric and Solar - Terrestrial Physics*, *162*, 192–202.

Gardner, C. S., Plane, J. M. C., Pan, W., Vondrak, T., Murray, B. J., & Chu, X. (2005). Seasonal variations of the Na and Fe layers at the South Pole and their implications for the chemistry and general circulation of the polar mesosphere. *Journal of Geophysical Research*, *110*, D10302. https://doi.org/10.1029/2004JD005670

Gerding, M., Daly, S., & Plane, J. M. C. (2019). Lidar soundings of the mesospheric nickel layer using $Ni(^3F)$ and $Ni(^3D)$ transitions. *Geophysical Research Letters*, *46*, 408–415. https://doi.org/10.1029/2018GL080701

Gettelman, A., Mills, M. J., Kinnison, D. E., Garcia, R. R., Smith, A. K., Marsh, D. R., et al. (2019). The Whole Atmosphere Community Climate Model version 6 (WACCM6). *Journal of Geophysical Research: Atmospheres*, *124*, 12,380–12,403. https://doi.org/10.1029/2019JD030943

Gómez Martín, J. C., Brooke, J. S. A., Feng, W. H., Höpfner, M., Mills, M. J., & Plane, J. M. C. (2017). Impacts of meteoric sulfur in the Earth's atmosphere. *Journal of Geophysical Research: Atmospheres*, *122*, 7678–7701. https://doi.org/10.1002/2017JD027218

Gómez Martín, J. C., Daly, S. M., Brooke, J. S. A., & Plane, J. M. C. (2017). Absorption cross sections and kinetics of formation of AlO at 298K. *Chemical Physics Letters*, *675*, 56–62. https://doi.org/10.1016/j.cplett.2017.02.087

Grebowsky, J. M., & Aikin, A. C. (2002). In situ measurements of meteoric ions. In E. Murad, & I. P. Williams (Eds.), *Meteors in the Earth's atmosphere* (pp. 189–214). Cambridge: Cambridge Univ. Press.

Heays, A. N., Bosman, A. D., & Dishoeck, E. F. V. (2017). Photodissociation and photoionisation of atoms and molecules of astrophysical interest. *Astronomy and Astrophysics*, *602*, A105.

Helmer, M., Plane, J. M. C., Qian, J., & Gardner, C. S. (1998). A model of meteoric iron in the upper atmosphere. *Journal of Geophysical Research*, *103*(D9), 10,913–10,925. https://doi.org/10.1029/97JD03075

Hurrell, J. W., Holland, M. M., Gent, P. R., Ghan, S., Kay, J. E., Kushner, P. J., et al. (2013). The community earth system model: A framework for collaborative research. *Bulletin of American Meteorological Society*, *94*(9), 1339–1360. https://doi.org/10.1175/BAMS-D-12-00121.1

Jessberger, E. K., Stephan, T., Rost, D., Arndt, P., Maetz, M., Stadermann, F. J., et al. (2001). Properties of interplanetary dust: Information from collected samples. In E. Grün, B. Å. S. Gustafson, S. Dermott, & H. Fechtig (Eds.), *Interplanetary Dust* (pp. 253–294). Berlin, Heidelberg: Springer. https://doi.org/10.1007/978-3-642-56428-4_6

Kopp, E. (1997). On the abundance of metal ions in the lower ionosphere. *Journal of Geophysical Research*, *102*(A5), 9667–9674. https://doi.org/10.1029/97JA00384

Krankowsky, D., Arnold, F., Wieder, H., & Kissel, J. (1972). The elemental and isotopic abundance of metallic ions in the lower *E*-region as measured by a cryogenically pumped quadrupole mass spectrometer. *International Journal of Mass Spectrometry and Ion Physics*, *8*(4), 379–390. https://doi.org/10.1016/0020-7381(72)83024-9

Langenberg, S., Carstens, T., Hupperich, D., Schweighoefer, S., & Schurath, U. (2020). Technical note: Determination of binary gas phase diffusion coefficients of unstable and adsorbing atmospheric trace gases at low temperature—Arrested Flow and Twin Tube method. *Atmospheric Chemistry and Physics*, *20*, 3669–3682.

Langowski, M. P., von Savigny, C., Burrows, J. P., Feng, W., Plane, J. M. C., Marsh, D. R., et al. (2015). Global investigation of the Mg atom and ion layers using SCIAMACHY/Envisat observations between 70 and 150 km altitude and WACCM-Mg model results. *Atmospheric Chemistry and Physics*, *15*(1), 273–295. https://doi.org/10.5194/acp-15-273-2015

Llewellyn, E. J., Lloyd, N. D., Degenstein, D. A., Gattinger, R. L., Petelina, S. V., Bourassa, A. E., et al. (2004). The OSIRIS instrument on the Odin spacecraft. *Canadian Journal of Physics*, *82*(6), 411–422. https://doi.org/10.1139/p04-005

Mangan, T. P., McAdam, N., Daly, S. M., & Plane, J. M. C. (2019). Kinetic study of Ni and NiO reactions pertinent to the Earth's upper atmosphere. *The Journal of Physical Chemistry. A*, *123*(2), 601–610. https://doi.org/10.1021/acs.jpca.8b11382

Manney, G. L., Lawrence, Z. D., Santee, M. L., Livesey, N. J., Lambert, A., & Pitts, M. C. (2015). Polar processing in a split vortex: Arctic ozone loss in early winter 2012/2013. *Atmospheric Chemistry and Physics*, *15*(10), 5381–5403. https://doi.org/10.5194/acp-15-5381-2015

Marsh, D. R., Janches, D., Feng, W., & Plane, J. M. C. (2013). A global model of meteoric sodium. *Journal of Geophysical Research: Atmospheres*, *118*, 11,442–11,452. https://doi.org/10.1002/jgrd.50870

Molina, L. T., & Molina, M. J. (1986). Absolute absorption cross sections of ozone in the 185 to 350 nm wavelength range. *Journal of Geophysical Research*, *91*(D13), 14,501–14,508. https://doi.org/10.1029/JD091iD13p14501

Molod, A., Takacs, L., Suarez, M., & Bacmeister, J. (2015). Development of the GEOS-5 atmospheric general circulation model: Evolution from MERRA to MERRA2. *Geoscientific Model Development*, *8*(5), 1339–1356. https://doi.org/10.5194/gmd-8-1339-2015

Nesvorný, D., Janches, D., Vokrouhlický, D., Pokorný, P., Bottke, W. F., & Jenniskens, P. (2011). Dynamical model for the zodiacal cloud and sporadic meteors. *The Astrophysical Journal*, *743*, 129.

Plane, J. M. C. (2003). Atmospheric chemistry of meteoric metals. *Chemical Reviews*, *103*(12), 4963–4984. https://doi.org/10.1021/cr0205309

Plane, J. M. C. (2004). A time-resolved model of the mesospheric Na layer: Constraints on the meteor input function. *Atmospheric Chemistry and Physics*, *4*(3), 627–638. https://doi.org/10.5194/acp-4-627-2004

Plane, J. M. C., Feng, W., Dawkins, E., Chipperfield, M. P., Höffner, J., Janches, D., & Marsh, D. R. (2014). Resolving the strange behavior of extraterrestrial potassium in the upper atmosphere. *Geophysical Research Letters*, *41*, 4753–4760. https://doi.org/10.1002/2014GL060334

Plane, J. M. C., Feng, W., & Dawkins, E. C. M. (2015). The mesosphere and metals: Chemistry and changes. *Chemical Reviews*, *115*(10), 4497–4541. https://doi.org/10.1021/cr500501m

Plane, J. M. C., Feng, W., Gómez Martín, J. C., Gerding, M., & Raizada, S. (2018). A new model of meteoric calcium in the mesosphere and lower thermosphere. *Atmospheric Chemistry and Physics*, *18*(20), 14,799–14,811. https://doi.org/10.5194/acp-18-14799-2018

Rollason, R. J., & Plane, J. M. C. (2000). The reactions of FeO with O_3, H_2, H_2O, O_2 and CO_2. *Physical Chemistry Chemical Physics*, *2*(10), 2335–2343. https://doi.org/10.1039/b000877j

Saran, D. V., Slanger, T. G., Feng, W., & Plane, J. M. C. (2011). FeO emission in the mesosphere: Detectability, diurnal behavior, and modeling. *Journal of Geophysical Research*, *116*, D12303. https://doi.org/10.1029/2011JD015662

Schlemmer, S., Luca, A., & Gerlich, D. (2003). Reactions of trapped ions with metal atoms: O_2^+ + Ni and NiN_2^+ + Ni. *International Journal of Mass Spectrometry*, *223*, 291–299.

Self, D. E., & Plane, J. M. C. (2003). A kinetic study of the reactions of iron oxides and hydroxides relevant to the chemistry of iron in the upper mesosphere. *Physical Chemistry Chemical Physics*, *5*(7), 1407–1418. https://doi.org/10.1039/b211900e

Smirnov, V. N. (2008). Rate constant of the gas-phase reaction between Fe atoms and CO_2. *Kinetics and Catalysis*, *49*(5), 607–609. https://doi.org/10.1134/S0023158408050017

Tobiska, W. K., Woods, T., Eparvier, F., Viereck, R., Floyd, L., Bouwer, D., et al. (2000). The SOLAR2000 empirical solar irradiance model and forecast tool. *Journal of Atmospheric and Solar - Terrestrial Physics*, *62*(14), 1233–1250. https://doi.org/10.1016/S1364-6826(00)00070-5

Unterguggenberger, S., Noll, S., Feng, W., Plane, J. M. C., Kausch, W., Kimeswenger, S., et al. (2017). Measuring FeO variation using astronomical spectroscopic observations. *Atmospheric Chemistry and Physics*, *17*(6), 4177–4187. https://doi.org/10.5194/acp-17-4177-2017

Viehl, T. P., Plane, J. M. C., Feng, W., & Höffner, J. (2016). The photolysis of FeOH and its effect on the bottomside of the mesospheric Fe layer. *Geophysical Research Letters*, *43*, 1373–1381. https://doi.org/10.1002/2015GL067241